



Self-introduction of carbon nitride quantum dots into carbon nitride planar structure for enhanced photocatalytic hydrogen production

Xue Ma, Hefa Cheng^{*}

MOE Key Laboratory for Earth Surface Processes, College of Urban and Environmental Sciences, Peking University, Beijing 100871, China

ARTICLE INFO

Keywords:

Photocatalytic hydrogen production
Carbon nitride quantum dots
Carbon nitride
Continuous π -conjugated bonds
In-plane electric fields

ABSTRACT

The separation efficiency and migration rate of photogenerated carriers are important factors determining the activity of photocatalysts. In this work, CN/CNQDs were prepared by self-introducing carbon nitride quantum dots (CNQDs) into the planar structure of carbon nitride (CN) using a novel photo-triggered self-assembly strategy. Different from conventional interfacial modification strategies based on van der Waals forces or hydrogen bonding, CN/CNQDs atomic junctions formed chemical bonds between the two components, which have stronger interfacial interactions and facilitate efficient carrier migration between the two components. The continuous π -conjugated structure of CN/CNQDs also provided unique conditions for carrier migration. In addition, the presence of in-plane electric field (IEF) in CN/CNQDs acted as a direct driving force for the migration of electrons and holes in the opposite directions, which greatly facilitates the separation and transfer of photogenerated carriers in CN/CNQDs. This work provides an atomic-level strategy for the construction of heterojunction photocatalyst systems.

1. Introduction

Combustion of fossil fuels have led to dramatic increase in the emissions of greenhouse gases, posing a serious threat to human survival and development [1,2]. In order to reduce the use of fossil fuels, it is necessary to develop new energy sources that can replace fossil fuels [3–5]. Hydrogen is an ideal clean energy source that can be used as an energy storage medium or carrier [6–8]. In the development of hydrogen energy, hydrogen production technology is one of the crucial aspects. Solar energy is a renewable and the most abundant source of clean energy [9–12]. Environmentally friendly and economical solar energy is one of the most promising energy sources to solve the energy shortages and environmental problems arising from fossil fuel combustion [13,14]. In particular, photocatalytic decomposition of water for hydrogen production is a potentially sustainable strategy that can meet future energy needs without damaging the environment. Photocatalytic hydrogen production is considered to be a highly promising technology for hydrogen production to address the problems of over-utilization, limited reserves, and negative environmental impacts associated with fossil fuels [15,16].

To promote the industrial implementation of photocatalytic hydrogen production technology, the development of highly efficient

photocatalysts remains the focus of current research [15,17,18]. Graphitic phase carbon nitride (CN) is a visible-light-responsive photocatalyst that possesses a unique two-dimensional structure, exceptional chemical stability, and adjustable electronic structure [19,20]. However, pure CN has limited photocatalytic activity as photogenerated electron-hole pairs recombine quickly. To enhance its photocatalytic properties, various nanoscale structures of CN have been developed [21, 22], including ultra-thin nanosheets [23], nanospheres [24], hollow structures [25], porous structures [23], and quantum dots [26]. Among these structures, carbon nitride quantum dots (CNQDs) have garnered significant attention due to their favorable photostability, low toxicity, adjustable surface chemistry, wide visible range response, and up-conversion luminescence effect [27,28].

Hu et al. synthesized water-soluble CNQDs with abundant active edges and oxygenated groups. These CNQDs exhibited blue single-photon light with a fluorescence quantum yield of 6.8% under UV excitation and green two-photon light in water with a wide excitation range of 750–900 nm in the near-infrared range [29]. Wang et al. prepared CNQDs using thermochemical etching and used them as a universal energy transfer component to enhance the photocatalytic activity of TiO₂ [30]. He et al. developed CNQDs that have controlled fluorescence emission wavelengths by changing the initial backbone of the

^{*} Corresponding author.

E-mail address: hefac@umich.edu (H. Cheng).

<https://doi.org/10.1016/j.apcatb.2023.123101>

Received 23 April 2023; Received in revised form 30 June 2023; Accepted 14 July 2023

Available online 17 July 2023

0926-3373/© 2023 Elsevier B.V. All rights reserved.

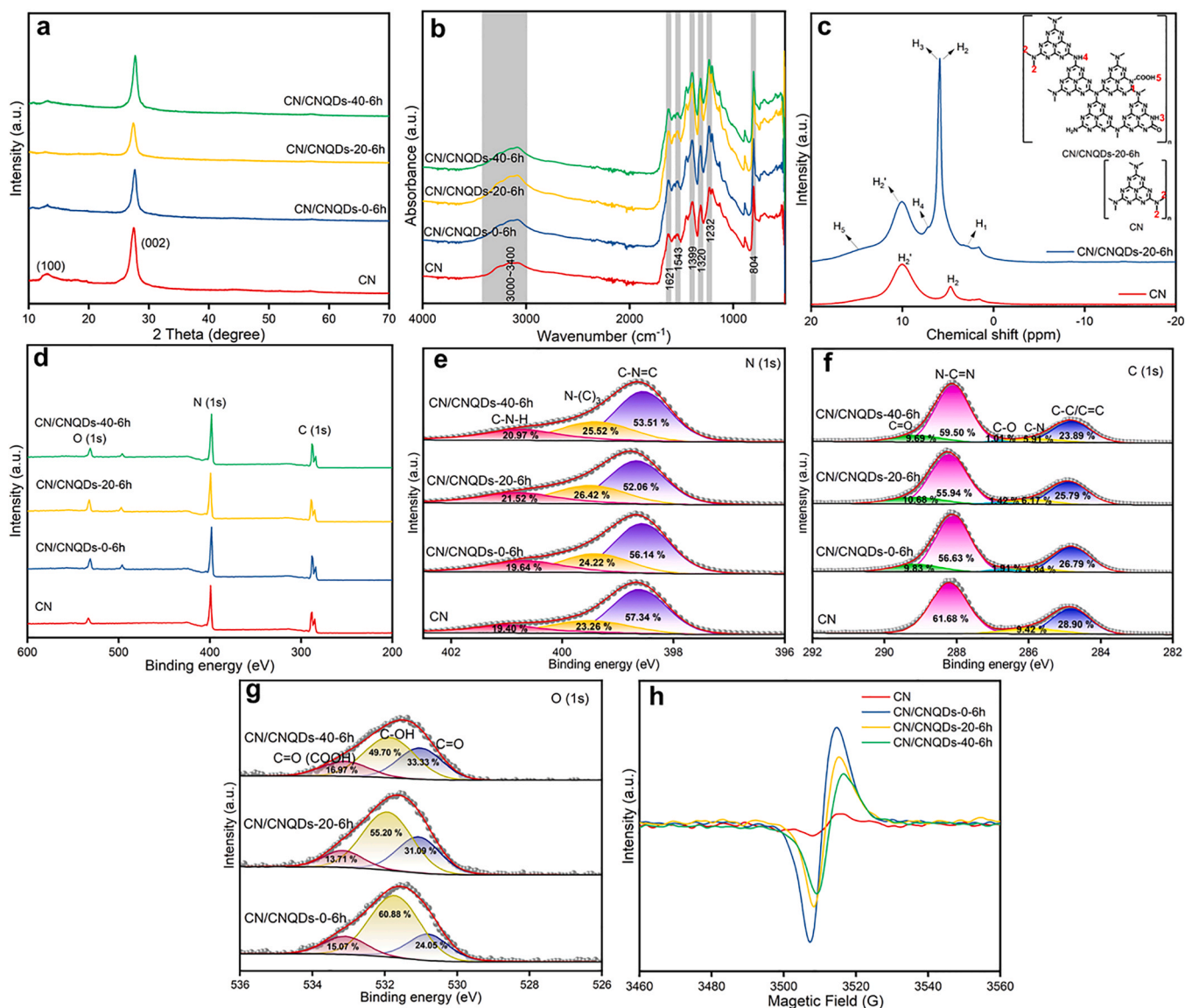


Fig. 1. XRD patterns (a) and FTIR spectra (b) of CN, CN/CNQDs-0–6 h, CN/CNQDs-20–6 h, and CN/CNQDs-40–6 h; (c) Solid-state ^1H nuclear magnetic resonance (NMR) and corresponding structural formula of CN and CN/CNQDs-20–6 h; XPS spectra of CN, CN/CNQDs-0–6 h, CN/CNQDs-20–6 h, and CN/CNQDs-40–6 h: (d) survey, (e) N (1s), (f) C (1s) and (g) O (1s); and EPR spectra (h) of CN, CN/CNQDs-0–6 h, CN/CNQDs-20–6 h, and CN/CNQDs-40–6 h.

tri-s-triazine structure, and showed that the electron-rich heterocycle of the pyrimidine donor effectively enhanced the electron conjugation effect [31]. These CNQDs have a large number of graphite or pyridine N atoms on the sp^2 hybridization plane and a large number of amine groups, along with a small number of carboxyl and hydroxyl groups on the terminal edges of their structures, which render them with unique physicochemical properties. Furthermore, CNQDs can also act as electron acceptors to facilitate charge transport. Thus, CNQDs can be used as efficient catalysts in photocatalytic applications.

Due to their unique structures and properties, CNQDs can be used as upconversion luminescence agents, i.e., converting the light with long wavelength to one with shorter wavelength to feed other substances for the generation of photogenerated carriers [32]. In addition, it can act as an electron acceptor, facilitating the separation of electrons and holes generated from other semiconductors. Taking advantage of this behavior, various semiconductor photocatalysts modified with CNQDs have been reported. For examples, Kumar et al. prepared F-doped TiO_2 modified with CNQDs, which exhibited a strong photochemical response at 500 nm [33]. CNQDs/ SnNb_2O_6 0D/2D nanocomposites prepared by Luo et al. exhibited enhanced hydrogen-producing photocatalytic

properties under visible light illumination, with the upconversion behavior of CNQDs rendering the nanocomposites with the ability to produce hydrogen at wavelength greater than 600 nm [34]. Ma et al. anchored CNQDs on the surface of CN nanosheets to form $\text{HJ-C}_3\text{N}_4$, which was 8.6 times more efficient at producing H_2O_2 in water than CN nanosheets [35]. These results demonstrate that depositing CNQDs on other semiconductors improve their photocatalytic activity by inhibiting the recombination of photogenerated carriers and broadening their range of light absorption. Nonetheless, the energy consumed by the carriers to cross the potential barriers between the CNQDs and other semiconductors is large. To achieve more efficient and rapid carrier transfer, it is necessary to induce the separation of photogenerated carriers around the photoexcitation sites in the two-dimensional semiconductor plane. Unfortunately, unlike atomic-scale doping, doping of external units unavoidably disrupts the original backbone structure of CN, compromising the photocatalytic activity. To the best of our knowledge, structures with CNQDs stitched seamlessly within the two-dimensional plane of CN have not been reported so far.

In this work, a new photo-triggered self-assembly mechanism was employed to implant CNQDs into the CN structural plane to form CN/

CNQDs with continuous π -conjugated bonds for unimpeded carrier transfer. The connection of the CNQDs and the CN component with different work functions results in a strong in-plane electric field (IEF) induced by the in-plane electron flow due to the different Fermi energy levels of each component. As a result, the IEF drives the orderly transfer of photogenerated electrons and holes to the CNQDs and CN ends, respectively, enabling the migration of electrons and holes in the opposite directions in the vicinity of the photoexcitation sites. The carboxyl groups in the CNQDs are hydrophilic and act as electron-accepting groups, serving as active sites for photocatalytic hydrogen production. In addition, with the amino and carboxyl groups act as electron donors and acceptors, respectively, an electron acceptor-donor (D-A) mechanism is formed within a small region, which facilitates the separation of photogenerated carriers. The present work provides a new way of thinking for the design and preparation of heterojunction photocatalysts.

2. Experimental

2.1. Photocatalyst preparation

Preparation of CN [36]: 5 g of melamine was calcined at 550 °C for 4 h, cooled to room temperature, then the resulting yellow product was thoroughly ground.

Preparation of exfoliated CN (ECN) [37]: 0.5 g of CN was added into 200 mL of ethanol-water mixture and ultrasonicated for 20 h. The solid was separated with centrifugation and then dried at 70 °C for 12 h. The resulting product was thoroughly ground.

Preparation of CNQDs [34]: 1.0 g of melamine and 0.8 g of sodium citrate were mixed well and carefully ground. The resulting powder was then added into 80 mL of ultrapure water and transferred into a 100 mL Teflon-lined stainless steel autoclave, which was subsequently heated at 180 °C for 2 h. After cooling, the resulting solution was dialyzed in pure water for 48 h using a dialysis membrane. The resulting dialysate was freeze-dried to obtain CNQDs.

Preparation of CN/CNQDs: 0.4 g of prepared CN and 0.02 g of CNQDs were added into 80 mL of ultrapure water, sonicated for 60 min and then illuminated under the light produced by a 300 W Xenon lamp for 0, 10, 20, 30, and 40 min to obtain CN/CNQDs-X (X indicates the time of light illumination). CN/CNQDs-X was then transferred into a 100 mL Teflon-lined stainless steel autoclave and heated at 180 °C for 2, 4, 6, and 8 h to obtain CN/CNQDs-X-Y h (Y indicates the heating time). ECN/CNQDs-20-6 h was also prepared similarly except that CN was replaced with ECN.

2.2. Photocatalytic hydrogen production

An on-line photocatalytic system for hydrogen production (Labsolar-6A, Perfectlight, Beijing, China) was used for photocatalytic water splitting experiments. The system utilized a 300 W Xenon lamp equipped with an AM 1.5 G filter as the simulated sunlight source. To 50 mL aqueous solution, 20 mg of photocatalyst was dispersed, along with 10 vol% triethanolamine (TEOA) as the sacrificial reagent, and 2.0 wt% Pt (in the form of H_2PtCl_6) as the co-catalyst. The temperature of the photocatalytic reactor was maintained at 5 °C by a connected refrigerated circulating bath. To ensure anoxic conditions, the photocatalytic system and the reactor were degassed for 30 min before light illumination. The produced hydrogen was analyzed by an online gas chromatograph equipped with a thermal conductivity detector (GC-910, Techcomp, Beijing, China), using argon as the carrier gas. The apparent quantum efficiency (AQE) for hydrogen production was evaluated using a 300 W Xenon lamp with a 420 nm band-pass filter, and was estimated as [38]:

$$\text{AQE} = \frac{N_e}{N_p} \times 100\% \quad (1)$$

where N_e is the number of electrons available for H_2 evolution and N_p is the number of incident photons in the photocatalytic system.

3. Results and discussion

3.1. Characterization of the prepared photocatalysts

X-ray diffraction (XRD) was employed to examine the crystal structure of the prepared photocatalysts. As depicted in Fig. 1a, there were two diffraction peaks present at 2θ values of 13.1° and 27.5°. These peaks corresponded to the (100) and (002) crystal planes of CN [39], respectively, and were attributed to the interplanar stacking of the triazine and aromatic units in the in-plane orientation [40]. Fig. S1a shows clear diffraction peaks of CNQDs, which are indicative of the superior crystallinity of CNQDs compared to CN [41]. The introduction of CNQDs into CN does not bring any obvious diffraction peak of CNQDs (Fig. S1b), which is due to the small amount of CNQDs added. Compared to that of CN, the intensity of the diffraction peak at 13.1° decreased after the introduction of CNQDs, which suggests that the small amount of CNQDs caused slight change in the structure of the in-plane triazine unit. The crystallinity of the CN/CNQDs increased with the hydrothermal synthesis time (Fig. S1). Additionally, the XRD patterns indicate that the introduction of CNQDs into the in-plane of CN barely changed the skeletal structure of CN.

The chemical structure of the prepared photocatalysts was analyzed using Fourier transform infrared spectroscopy (FTIR) spectra (Fig. 1b and Fig. S2). The peak around 804 cm^{-1} was attributed to the bending of the out-of-plane skeleton of the triazine ring [42], while those at 1232, 1320, and 1399 cm^{-1} corresponded to the stretching of the aromatic sp^3 C-N bonds [43]. The peak at 1621 cm^{-1} was associated with the stretching vibrations of sp^2 C=N [43,44]. The broad absorption band observed between 3000 and 3400 cm^{-1} was considered to be N-H stretching vibrations and O-H bands [45]. On the FTIR spectra of CNQDs (Fig. S2b), the peaks at 785, 841, and 1583 cm^{-1} belonged to the bending vibration of C-NH-C [46], typical breathing mode of triazine units [46], and C=N stretching mode in heterocyclic CN [47], respectively, which confirm the CN backbone structure. The peak observed at 906 cm^{-1} resulted from the out-of-plane bending vibration of aromatic C-H, suggesting the existence of pyrimidine component in the CNQDs [46]. The peak observed at 1302 cm^{-1} was assigned to the vibrations of the C-O bond in the C-OH group [48]. Additionally, the peaks at 1390 cm^{-1} and 1669 cm^{-1} corresponded to the bending mode of the OH group and the stretching mode of the C=O bond in the -COOH group, respectively [41].

Solid-state ^1H nuclear magnetic resonance (NMR) characterization was performed to further investigate the structural composition of CN/CNQDs (Fig. 1c). A peak at approximately 1.56 ppm appeared in both CN and CN/CNQDs-20-6 h, which is attributed to the water molecules adsorbed on their surface. The peaks located at 4.69 (H_2) and 10.00 (H_2^+) ppm in CN were associated with the non-hydrogen bonded NH_2 group and the NH_2 group involved in hydrogen bonding, respectively [49]. In comparison to CN, three new peaks were observed in CN/CNQDs-20-6 h, at 3.08 (H_1), 7.20 (H_4), and 14.40 (H_5) ppm, which belong to C-H, bridged NH groups, and COOH groups, respectively, due to the presence of CNQDs [49]. The position of the peak from the non-hydrogen bonded NH_2 group shifted to the left and its intensity increased significantly. This is because the edges of CNQDs contained many NH_2 groups that were exposed to the edges of CN/CNQDs after seamless splicing with CN, indicating that the NH_2 groups in CNQDs were not involved in the reaction after the implantation of CNQDs into CN. However, no peak was observed at the position of H_4 on the solid-state ^1H NMR spectrum of CN/CNQDs-0-6 h (Fig. S3), indicating the absence of bridged NH groups in CN/CNQDs-0-6 h. This is attributed to the fact that CN and CNQDs could not combine together in the absence of light illumination, instead, CNQDs would simply attach to the

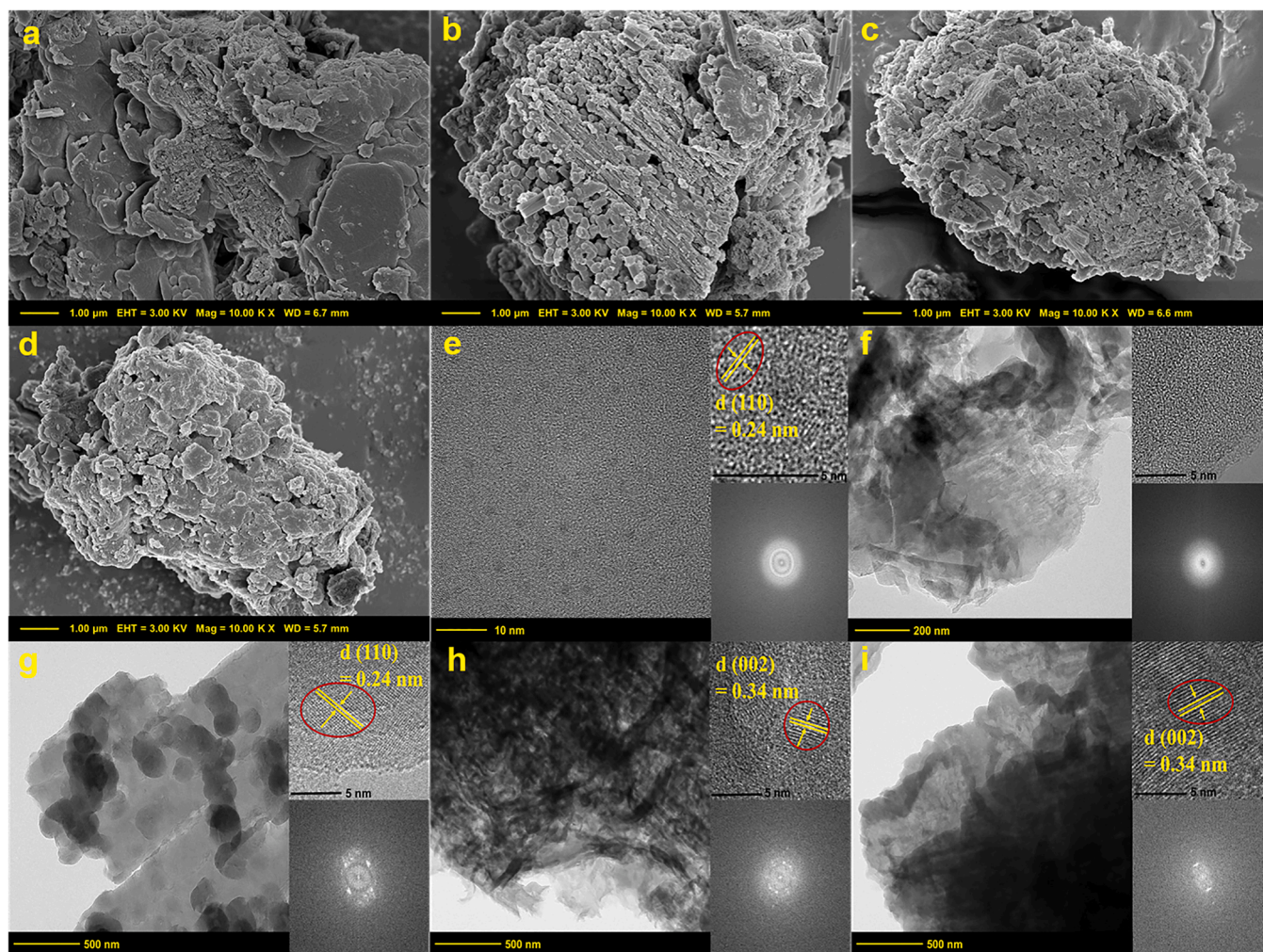


Fig. 2. SEM micrographs of (a) CN, (b) CN/CNQDs-0-6 h, (c) CN/CNQDs-20-6 h, and (d) CN/CNQDs-40-6 h; TEM micrographs of (e) CNQDs, (f) CN, (g) CN/CNQDs-0-6 h, (h) CN/CNQDs-20-6 h, and (i) CN/CNQDs-40-6 h.

surface of CN surface. In contrast, CN/CNQDs-20-6 h, which has a rather low content of CNQDs, showed a small peak at the position of H₄ (Fig. 1c), which confirms that CN and CNQDs were chemically bonded after light illumination. This is consistent with the findings of a previous study, which reported that photogenerated electrons under light could trigger the dehydration reaction between amino groups and hydroxyl groups, thereby generating bridged NH groups [41]. Further details on the chemical bonding between CN and CNQDs are discussed later.

X-ray photoelectron spectroscopy (XPS) was utilized to confirm the structural composition of the photocatalysts prepared, namely CN, CN/CNQDs-0-6 h, CN/CNQDs-20-6 h, and CN/CNQDs-40-6 h. The survey spectra showed strong signal peaks for C (1s) and N (1s) (Fig. 1d). The peaks observed on the N (1s) spectra at 401.0, 399.5, and 398.6 eV (Fig. 1e) were attributed to C-N-H, N-(C)₃, and C-N = C, respectively [50]. The C (1s) spectra exhibited peaks at 288.2, 285.9, and 284.2 eV (Fig. 1f), which corresponded to the N-C=N, C-N, and C-C/C=C in CN, respectively [51]. The intensity of the peaks of both hydroxyl and carboxyl groups decreased after the introduction of CNQDs to form CN/CNQDs, due to the dehydration reaction induced by light illumination. The O (1s) spectra displayed peaks at 533.1, 531.8, and 530.8 eV (Fig. 1g), which were assigned to C=O (COOH), C-OH, and C=O, respectively [52]. These results confirm the successful implantation of CNQDs into the structure of CN. Meanwhile, the duration of calcination treatment did not have significant impact on the structure of CN/CNQDs (Fig. S4).

Electron paramagnetic resonance (EPR) spectra were used to test the spin states of unpaired electrons in the four photocatalysts (Fig. 1h). CN/CNQDs-0-6 h exhibited a significantly stronger peak than CN, CN/CNQDs-20-6 h, and CN/CNQDs-40-6 h. Additionally, CN/CNQDs-20-6 h had a more intense peak than CN/CNQDs-40-6 h. These results suggest that introducing CNQDs into the planar structure of CN can increase the number of unpaired electrons. However, the number of unpaired electrons decreased with the duration of light illumination in the synthesis process, due to the connection of CN and CNQDs. This is attributed to the formation of chemical bonds between CN and the CNQDs introduced into the planar structure of CN under light illumination, which reduces the number of unpaired electrons.

The microstructures of CN, CNQDs, CN/CNQDs-0-6 h, CN/CNQDs-20-6 h, and CN/CNQDs-40-6 h were examined with field-emission scanning electron microscopy (SEM) and field-emission high resolution transmission electron microscopy (TEM) (Fig. 2). The SEM image indicates that CN has a stacked lamellar structure (Fig. 2a). After the addition of CNQDs to form CN/CNQDs-0-6 h (Fig. 2b), some small spherical particles were visible in the middle of the lamellar structure, which are attributed to the added CNQDs. Upon further addition of CNQDs to CN and 20 min of light illumination, the small spherical particles disappeared, while small pores appeared on the surface of the lamellar structure of the CN/CNQDs-20-6 h formed (Fig. 2c). This probably resulted from the dehydration reaction between the amino groups of CN and the hydroxyl groups of CNQDs under light

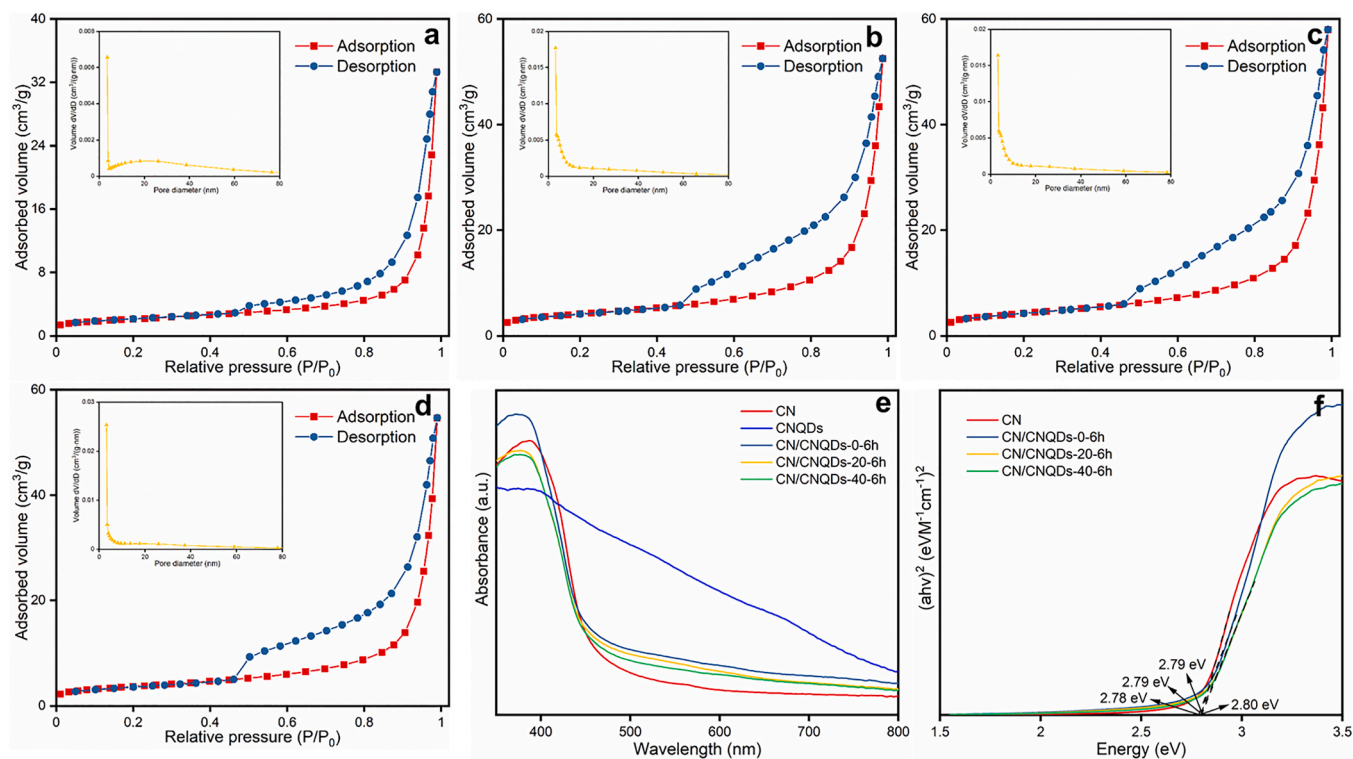


Fig. 3. Nitrogen adsorption-desorption isotherms and pore size distribution of (a) CN, (b) CN/CNQDs-0-6 h, (c) CN/CNQDs-20-6 h, and (d) CN/CNQDs-40-6 h; and UV-Vis DRS spectra (e) and determination of the band gaps (f) of CN, CNQDs, CN/CNQDs-0-6 h, CN/CNQDs-20-6 h, and CN/CNQDs-40-6 h. The pore size distribution was calculated from the desorption branch of isotherm by the Barrett-Joyner-Halenda (BJH) method.

illumination, causing CNQDs to splice into the planar structure of CN [41]. After 40 min of light exposure, the CN/CNQDs-40-6 h formed possessed a larger blocky structure (Fig. 2d). The prolonged light exposure allowed more CNQDs to splice into the planar structure of CN, leading to the formation of a blocky structure. The TEM image of CNQDs shows that they occurred as small particles of approximately 2 nm with a lattice spacing of 0.24 nm (Fig. 2e), which corresponds to the (110) lattice plane of the CNQDs. In contrast, CN appeared to have a thin lamellar structure with no obvious lattice fringe (Fig. 2f). Compared to the amorphous structure of the prepared CN, CNQDs had much better crystallinity, which resulted in the clear lattice stripes on the TEM image. The difference in crystallinity of the prepared CN and CNQDs revealed with TEM is consistent with their XRD patterns (Fig. 1a). After the addition of CNQDs to CN, the small spherical particles were attached to the surface of the large lumpy particles (Fig. 2g). These small particles were CNQDs with a lattice spacing of 0.24 nm [35], while the large lump without lattice fringe was CN. These results demonstrate that CNQDs simply attached to the surface of CN in the absence of light illumination and did not implant into the CN structure. In contrast, the small particles disappeared and the bulk CN became flaky after 20 min of light illumination (Fig. 2h), while small holes showed up on the surface and lattice fringes with a spacing of 0.34 nm appeared in localized areas, indicating splicing of CNQDs into the planar structure of CN. After 40 min of light illumination (Fig. 2i), the small holes disappeared, and the CN/CNQDs-40-6 h exhibited a mere lamellar morphology. The local lattice fringes had a spacing of 0.34 nm, which corresponds to the (002) crystal plane of the CNQDs [27]. These results indicate that more CNQDs spliced into the CN structure with prolonged light illumination.

Figs. 2b and 2g shows that the CNQDs in the CN/CNQDs-0-6 h had a spherical structure, and they were attached to the surface of CN but did not implant in its structure. On Fig. 2g, the CNQDs had oriented lattice fringes over large areas, whereas there was no specific lattice orientation on Fig. 2h, indicating that the CN edges were randomly attached to the CNQDs. As the time of light illumination increased, more CN and CNQDs

bonded, producing a larger range of lattice fringes and a uniform distribution of crystal planes over larger area. This phenomenon is indicative of the occurrence of recrystallization after light illumination. Prolonged light exposure resulted in thicker particles and disappearance of small holes between the particles, leading to the formation of large lumps (Figs. 2d and 2i). These results are indicative of better crystallization of the sample, with more CNQDs spliced into the CN structure, and suggest that illumination promotes the splicing of CNQDs into the planar structure of CN by facilitating the dehydration reaction between amino and hydroxyl groups. The distribution of C, N, and O elements in CN, CN/CNQDs-0-6 h, CN/CNQDs-20-6 h, and CN/CNQDs-40-6 h was analyzed using energy dispersive X-ray (EDS) mapping (Fig. S6), and their elemental composition was as expected.

To further confirm that light can promote the implantation of CNQDs into the structure of CN, the CNQDs were directly illuminated to observe the change in their sizes (Fig. S5). In the absence of light illumination, the sizes of CNQDs were approximately 2 nm (Fig. S5a), while they increased to around 4 nm after 20 min of light illumination (Fig. S5b). The sizes of CNQDs increased further to about 9 nm after 60 min of light illumination (Fig. S5c). These results consistently indicate that light promotes the binding between CNQD particles. It has been shown that photogenerated electrons under light can trigger dehydration reaction between amino and hydroxyl groups, thereby promoting the bonding between CNQDs [41]. Since CN contains amino groups while CNQDs contain hydroxyl groups, their chemical splicing under light illumination allowed for the integration of CNQDs into the structure of CN.

Fig. 3a-d and Fig. S7 display the N₂ adsorption-desorption isotherms and pore size distribution of the prepared photocatalysts. The Brunauer-Emmett-Teller (BET) surface areas of CN, CN/CNQDs-0-6 h, CN/CNQDs-20-6 h, CN/CNQDs-40-6 h, CN/CNQDs-20-4 h, and CN/CNQDs-20-8 h were determined to be 7.34, 14.69, 15.13, 12.85, 32.07, and 12.5 m²/g, respectively. The introduction of CNQDs on the surface of CN caused doubling of the BET surface area (Fig. 3b). After implantation of the CNQDs into the planar structure of CN, the BET

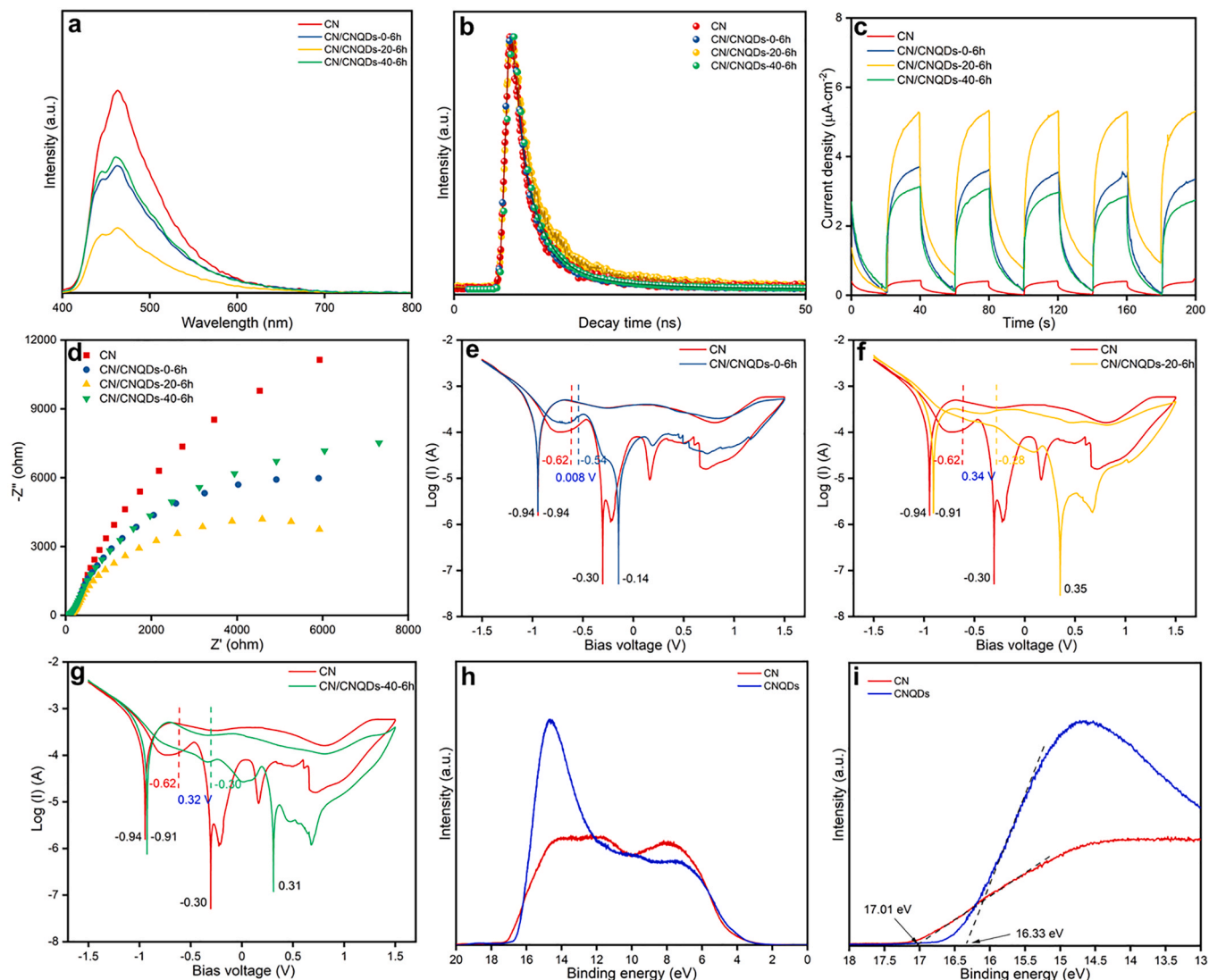


Fig. 4. (a) PL spectra, (b) time-resolved PL spectra, (c) photocurrent response spectra, and (d) EIS spectra of CN, CN/CNQDs-0-6 h, CN/CNQDs-20-6 h, and CN/CNQDs-40-6 h; (e) log I - V curves of CN and CN/CNQDs-0-6 h, (f) log I - V curves of CN and CN/CNQDs-20-6 h, and (g) log I - V curves of CN and CN/CNQDs-40-6 h; and UPS spectra (h) and the obtained electron cutoff (i) of CN and CNQDs.

surface area further increased slightly due to the occurrence of small pores on the surface of CN/CNQDs-20-6 h (Fig. 3c). However, prolonged light illumination resulted in the formation of larger structural units with the binding of more CNQDs and CN, leading to reduction in BET surface area (Fig. 3d). Meanwhile, comparison of the N_2 adsorption-desorption isotherms of CN/CNQDs-20-4 h, CN/CNQDs-20-6 h, and CN/CNQDs-20-8 h reveals that increasing the time of calcination treatment brought reduction in their BET surface areas (Fig. S7).

Figs. 3e, 3f, and Fig. S7 display the UV-Vis diffuse reflectance spectroscopy (DRS) spectra of the photocatalysts prepared and the corresponding calculated band gaps. The absorption spectrum of CNQDs covers the entire visible range, although the absorption ranges of these photocatalysts do not differ significantly (Fig. 3e). The calculated band gaps for CN, CN/CNQDs-0-6 h, CN/CNQDs-20-6 h, CN/CNQDs-40-6 h, CN/CNQDs-20-4 h, and CN/CNQDs-20-8 h were 2.80, 2.78, 2.79, 2.79, 2.82, and 2.84 eV, respectively (Fig. 3f and Fig. S8b). These results indicate that the introduction of CNQDs into the CN structure had negligible impact on its band gap, probably due to the rather low contents of CNQDs. The Mott-Schottky curves (Fig. S9) and the XPS valence band potential (VB-XPS) (Fig. S10) were used to investigate the conduction and valence band potentials of these photocatalysts. The

conduction band potentials of CN and CN/CNQDs-20-6 h, relative to Ag/AgCl, were -1.55 and -1.56 V, respectively, corresponding to -1.35 and -1.36 V with respect to NHE [53]. The valence band potentials of CN and CN/CNQDs-20-6 h determined by VB-XPS were 1.25 and 1.23 eV, respectively. Thus, the band gaps of these two samples were 2.80 and 2.79 eV, respectively, which are consistent with the band gaps determined from UV-Vis DRS spectra.

The separation and transfer of photogenerated carriers in the photocatalysts prepared were evaluated using photoluminescence (PL), photocurrent response, and electrochemical impedance spectroscopy (EIS). Fig. 4a and Fig. S11a display the PL spectra of CN, CN/CNQDs-0-6 h, CN/CNQDs-20-6 h, CN/CNQDs-40-6 h, CN/CNQDs-20-4 h, and CN/CNQDs-20-8 h (excited at 365 nm). CN/CNQDs-0-6 h, CN/CNQDs-20-6 h, and CN/CNQDs-40-6 h exhibited lower fluorescence intensity than CN due to the presence of CNQDs (Fig. 4a), which prevent the recombination of photogenerated carriers. Notably, CN/CNQDs-20-6 h displayed the lowest fluorescence intensity, suggesting that implantation of CNQDs into CN structure effectively inhibits the recombination of photogenerated carriers. Nonetheless, prolonged light illumination time during synthesis resulted in the formation of large bulk nanosheets (CN/CNQDs-40-6 h), which are not conducive to carrier mobility and

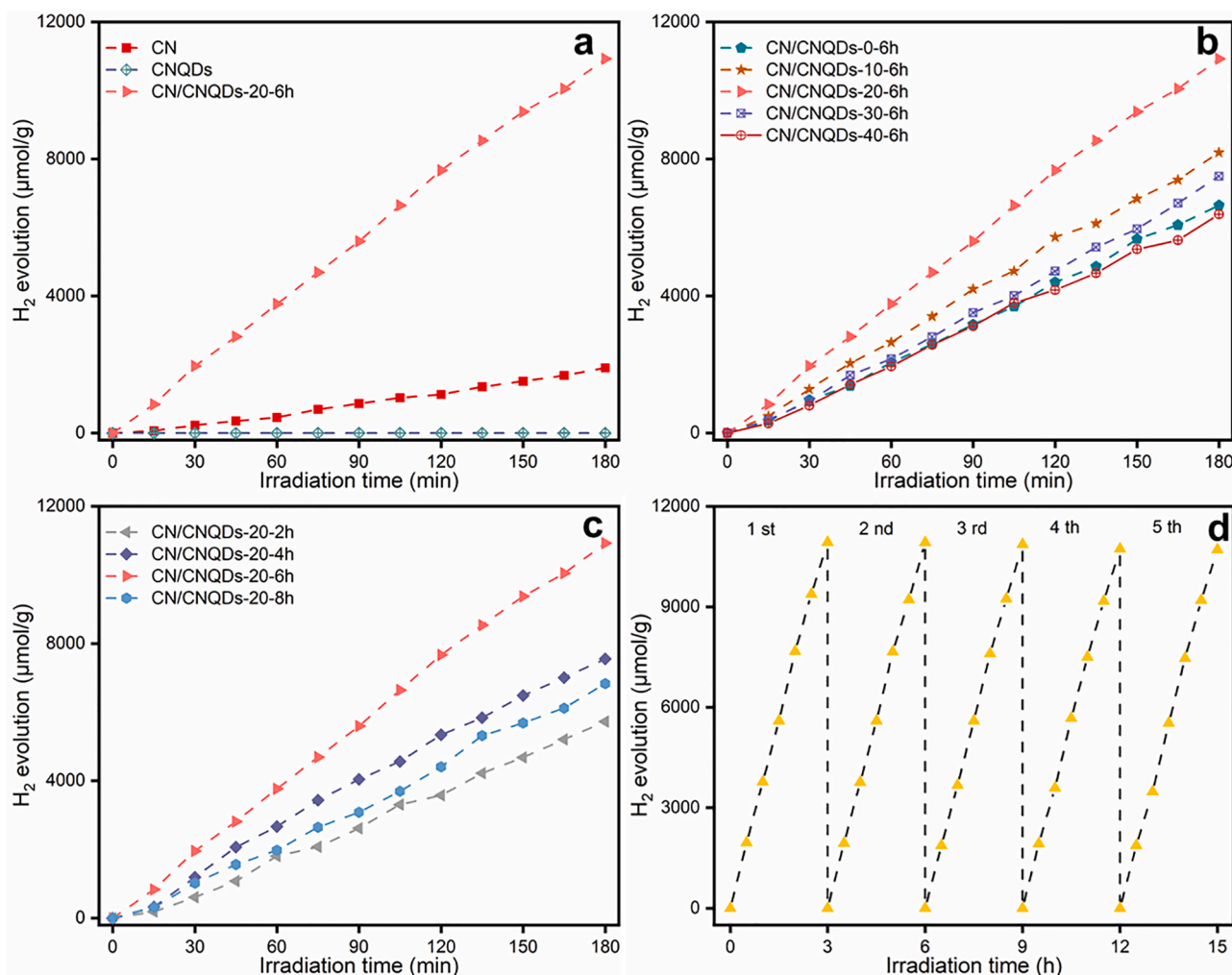


Fig. 5. Photocatalytic hydrogen production under simulated sunlight illumination: (a) photocatalytic activity of CN, CNQDs, and CN/CNQDs-20-6 h; (b) photocatalytic activity of CN/CNQDs-0-6 h, CN/CNQDs-10-6 h, CN/CNQDs-20-6 h, CN/CNQDs-30-6 h, and CN/CNQDs-40-6 h; (c) photocatalytic activity of CN/CNQDs-20-2 h, CN/CNQDs-20-4 h, CN/CNQDs-20-6 h, and CN/CNQDs-20-8 h; and (d) reuse of CN/CNQDs-20-6 h over five consecutive cycles.

separation. In addition, CN/CNQDs-20-6 h had lower fluorescence intensity compared to CN/CNQDs-20-4 h and CN/CNQDs-20-8 h (Fig. S11a), indicating that a controlled calcination time of 6 h is optimal. Time-resolved transient PL spectra of CN and CN/CNQDs-20-6 h were used to further investigate the carrier dynamics (Fig. 4b). The calculated radiative recombination lifetimes for CN, CN/CNQDs-0-6 h, CN/CNQDs-20-6 h, and CN/CNQDs-40-6 h were 5.46, 5.61, 6.96, and 5.72 ns, respectively. The radiative recombination lifetime of CN increased with the introduction of CNQDs. Compared to the case of simple attachment of CNQDs to CN, the radiative recombination lifetime was higher when the CNQDs were implanted into the CN structure. However, the radiative recombination lifetime decreased with the light illumination time during synthesis, which resulted in larger bulk structure with the bonding of more CNQDs with the CN phase. These results indicate that controlling the light illumination time during synthesis is necessary for obtaining photocatalysts with optimum activity. CN/CNQDs-20-6 h exhibited the longest fluorescence lifetime, suggesting that introducing CNQDs into CN structure greatly improves the separation of excited-state charge carriers, rendering it with superior photocatalytic activity.

Photocurrent response spectra of CN, CN/CNQDs-0-6 h, CN/CNQDs-20-6 h, and CN/CNQDs-40-6 h were recorded to evaluate their charge transfer efficiency (Fig. 4c and Fig. S11b). Notably, CN/CNQDs-20-6 h showed significantly higher photocurrent response than the other

photocatalysts, indicating that it has superior charge separation capability. In addition, the arc radius of CN/CNQDs-20-6 h was much smaller than those of the other photocatalysts (Fig. 4d and Fig. S11c), suggesting that it has better electrical conductivity and electron mobility. CNQDs possess better carrier transfer efficiency than CN, as indicated by the stronger photocurrent response and smaller arc radius compared to those of CN (Fig. S13j and S13k). Overall, the presence of CNQDs in the CN structure accelerates the separation and transfer of photogenerated carriers, and is beneficial for photocatalytic activity.

To further investigate the separation and transfer mechanism of photogenerated carriers after the implantation of CNQDs into CN structure, log *I*-*V* curves, which are based on cyclic voltammetry, were used to measure the intensity of IEF [54]. The central potentials (*V*_i) of CN/CNQDs-0-6 h, CN/CNQDs-20-6 h, and CN/CNQDs-40-6 h relative to CN were observed to shift due to the formation of IEF between the different components. For pure CN, *V*_i (−0.94 V, −0.30 V) is centered at −0.62 V, which comes from the IEF between the CN and the ITO substrate. For CN/CNQDs-0-6 h, *V*_i (−0.94 V, −0.14 V) is centered at −0.54 V, with a potential shift of 0.008 V. The *V*_i (−0.91 V, 0.35 V) of CN/CNQDs-20-6 h is centered at −0.28 V, and the potential shift of 0.34 V is contributed by the IEF. Similarly, the *V*_i (−0.91 V, 0.31 V) of CN/CNQDs-40-6 h is centered at −0.30 V, and the potential shift of 0.32 V is contributed by the IEF. These results demonstrate that combination of CNQDs and CN can significantly enhance the strength of the

IEF, especially when CNQDs are implanted into the planar structure of CN. The stronger IEF provides a greater driving force for the separation and transfer of electrons and holes, which effectively promotes the separation and transfer of carriers.

The creation of IEF was investigated using ultraviolet photoelectron spectroscopy (UPS) (Fig. 4h). The work function was found to be 4.21 and 4.89 eV for CN and CN/CNQDs-20–6 h, respectively, from subtracting the respective value of electron cut-off (17.01 and 16.33 eV) from the photon energy (21.22 eV) (Fig. 4i) [55]. The Fermi energy levels of CN and CN/CNQDs-20–6 h were further determined to be -0.23 and 0.45 eV, respectively. That is, the introduction of CNQDs into the CN plane led to significant reduction in the Fermi energy level of CN/CNQDs-20–6 h. The continuous contact via π -conjugate bonds within the formed 2D nanosheets allows electrons to flow from the higher Fermi energy levels to the lower Fermi energy levels and reach equilibrium. This results in negatively charged CNQDs end and positively charged CN components at the lower and higher Fermi energy levels, respectively, leading to the formation of IEF.

3.2. Photocatalytic hydrogen production

Fig. 5a compares the hydrogen production performance of CN, CNQDs, and CN/CNQDs-20–6 h. With the largest work function among noble metals, Pt can play an important role in capturing photogenerated electrons, providing active sites for H^+ reduction, and reducing the reaction energy barrier to promote photocatalytic hydrogen production [25]. Thus, Pt was used as a co-catalyst in the experiments to further improve of the performance of photocatalytic hydrogen production. During the 180 min of simulated sunlight illumination, CNQDs produced almost no hydrogen, while the production of hydrogen in the presence of CN and CN/CNQDs-20–6 h increased linearly with the illumination time. The photocatalytic hydrogen production rates in the presence of CN and CN/CNQDs-20–6 h were 1902.9 and 10921.8 $\mu\text{mol/g}$, respectively, and the calculated AQE values of hydrogen production at 420 nm were 0.46% and 6.74%, respectively. This drastic difference is attributed to the presence of CNQDs in the heterostructure plane of CN, which facilitates carrier transfer due to the continuous π -conjugated bonds. The strong IEF induced in the plane of CN/CNQDs-20–6 h drives the orderly transfer of photogenerated electrons and holes, which enables the migration of electrons and holes in the opposite directions near the photoexcitation site. This effectively inhibits the recombination of photogenerated carriers and accelerates their transfer rates, rendering CN/CNQDs-20–6 h with excellent photocatalytic hydrogen production activity.

Fig. 5b compares the hydrogen production activity of CN/CNQDs photocatalysts. Within 180 min of simulated sunlight illumination, the photocatalytic hydrogen production rates in the presence of CN/CNQDs-0–6 h, CN/CNQDs-10–6 h, CN/CNQDs-20–6 h, CN/CNQDs-30–6 h, and CN/CNQDs-40–6 h reached 6646.7, 8187.5, 10921.8, 9847.9, and 8057.6 $\mu\text{mol/g}$, respectively. A volcano-shape curve was observed for the activity of the photocatalyst with respect to the illumination time during the synthesis process, with the one with 20 min of light illumination exhibiting the highest activity. On one hand, the implantation of suitable amount of CNQDs into the structure of CN brought by light illumination increases its specific surface area and enhances the separation efficiency and transfer rate of the photogenerated carriers. On the other hand, prolonged light illumination introduces excessive amount of CNQDs into CN and causes formation of larger bulk structure, which not only decreases the specific surface area, but also increases the recombination rate of photogenerated carriers.

Fig. 5c compares the hydrogen production activity of CN/CNQDs-20–2 h, CN/CNQDs-20–4 h, CN/CNQDs-20–6 h, and CN/CNQDs-20–8 h. The photocatalytic hydrogen production increased initially with the calcination time, with a maximum of 10921.8 $\mu\text{mol/g}$ occurred when the calcination time was 6 h (CN/CNQDs-20–6 h), then decreased with further increase in the calcination time. This trend is consistent

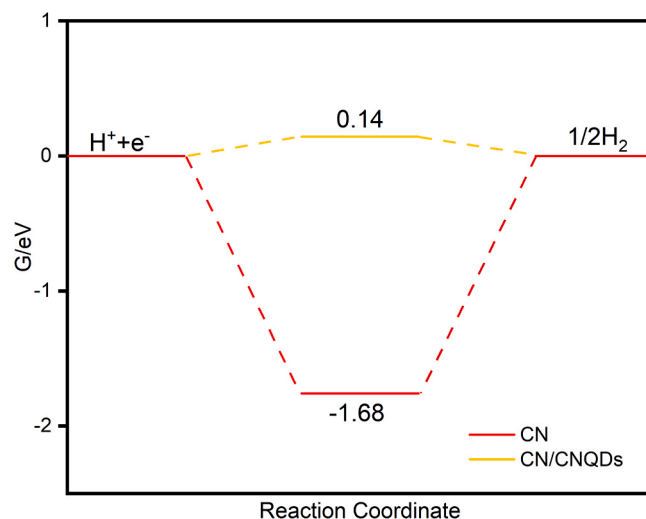


Fig. 6. Theoretically calculated Gibbs free energy profiles for hydrogen production catalyzed by CN and CN/CNQDs.

with the results of PL spectra (Fig. S11a), and is attributed to the change in the efficiency of photogenerated carrier separation influenced by the calcination treatment.

Since the CNQDs implanted in the CN/CNQDs photocatalysts are chemically bonded to CN, they are expected to be more chemically stable than the composite photocatalyst. Nonetheless, it is important to evaluate their stability and reusability. Fig. 5d shows the photocatalytic hydrogen production performance of CN/CNQDs-20–6 h over five cycles of use. The results indicate that the photocatalytic activity of CN/CNQDs-20–6 h barely changed over the five use cycles. In addition, XRD and FTIR spectra show little change for the used photocatalyst (Fig. S12). These results consistently demonstrate that the CN/CNQDs-20–6 h photocatalyst is highly stable and can be reused for photocatalytic hydrogen production.

To further improve the activity of the CN/CNQDs photocatalyst, ECN was prepared by stripping CN into thin layers, and ECN/CNQDs-20–6 h was subsequently synthesized by implanting CNQDs into ECN. Fig. S13a indicates that the intensity of the (002) diffraction peak associated with the interlayer stacking was obviously weakened after the exfoliation of CN, demonstrating that the multilayered CN was successfully exfoliated. After the combination of ECN and CNQDs to form ECN/CNQDs-20–6 h, the XRD diffraction peak intensity increased significantly, indicating the crystallinity of ECN was improved with the introduction of CNQDs. FTIR spectra show that the structure of CN was not destroyed after being exfoliated into ECN (Fig. S13b). The BET surface areas of ECN and ECN/CNQDs-20–6 h were determined to be 18.41 and 26.75 m^2/g , respectively (Fig. S13c and S13d), which are much higher than those of CN (7.34 m^2/g) and CN/CNQDs-20–6 h (15.13 m^2/g). Exfoliating CN into thin layers greatly increased the specific surface area of CN/CNQDs, which is expected to provide more reactive sites and facilitate hydrogen generation. SEM images show that the ECN particles were much thinner and were composed of less layers, while the surface of ECN/CNQDs-20–6 h had many small holes (Fig. S13e and S13f), which would facilitate the transport of electrons. No lattice stripes were found on the TEM image of ECN, while that of ECN/CNQDs-20–6 h had clear lattice stripes due to the implantation of CNQDs in the ECN (Fig. S13g and S13h). ECN exhibited lower PL intensity, higher photocurrent response, and smaller arc radius compared to CN (Fig. S13i, S13j, and S13k), which are indicative of better electrical conductivity and electron mobility. Among the photocatalysts evaluated, ECN/CNQDs-20–6 h showed the lowest PL intensity, the highest photocurrent response, and the smallest arc radius, indicating it has the best separation ability of charge carriers. Fig. S13l shows that the photocatalytic hydrogen production in the presence of

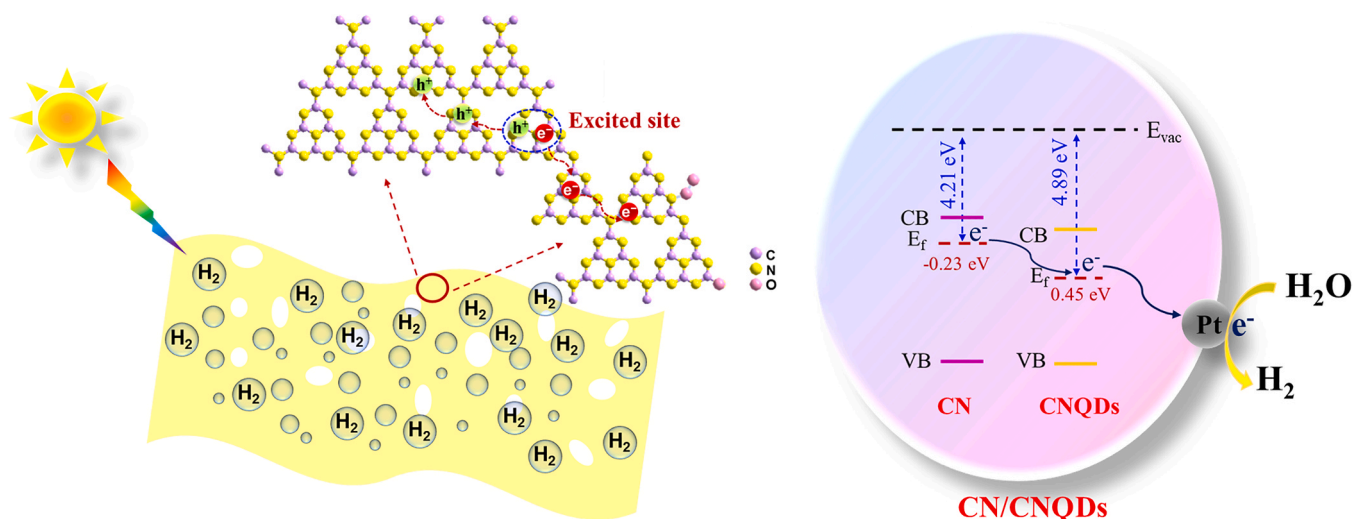


Fig. 7. Probable electron transfer pathways of hydrogen production in the presence of CN/CNQDs-20–6 h as the photocatalyst and Pt as the co-catalyst under simulated sunlight illumination.

CN, ECN, CN/CNQDs-20–6 h and ECN/CNQDs-20–6 h were 1902.9, 2492.8, 10921.8, and 12263.2 $\mu\text{mol/g}$, respectively, after 180 min, confirming that ECN/CNQDs-20–6 h has the highest photocatalytic activity. Together, these results demonstrate that the photocatalytic hydrogen production activity of CN/CNQDs can be further improved by exfoliating the CN into thin layers. The hydrogen production activity of the CN/CNQDs-20–6 h photocatalysts prepared in this work, particular after exfoliation of CN, is higher than most of the CN-based ones reported in the literature (Table S1).

3.3. Insights obtained by DFT calculations

In order to investigate the photocatalytic hydrogen production capability of CN and CN/CNQDs, Gibbs free energy barrier curves were calculated (Fig. 6), with the structure models of CN and CN/CNQDs shown in Fig. S14 and Fig. S15, respectively. The $\Delta G(\text{H}^*)$ on CN and CN/CNQDs were calculated to be -1.68 and 0.14 eV, respectively, indicating that the adsorption of H^* on CN is very strong while the H^* adsorbed on the surface of CN/CNQDs can be easily converted into H_2 . Thus, the theoretically calculated Gibbs free energy profiles support that CN/CNQDs has much better performance in photocatalytic hydrogen production than CN alone.

3.4. Mechanism of photocatalytic hydrogen production

Constructing atomic junctions within the CN plane allows the formation of atomic-scale charge transport channels, which significantly improves the transfer rate of photogenerated carriers. This enables more internal carriers to migrate to the active sites on photocatalyst surface, increasing their participation in redox reactions. The atomic junctions of CN and CNQDs create chemical bonds between the components, resulting in stronger interfacial interactions than those achieved by conventional interfacial modulation based on the van der Waals forces. The chemical bonds facilitate the effective directional migration of photogenerated carriers between the components. Additionally, the continuous π -conjugated bonds between the CNQDs and the CN create favorable conditions for carrier migration.

Efficient carrier separation and transfer in photocatalysts rely heavily on the separation efficiency of electron-hole pairs. One effective strategy to promote this is the introduction or enhancement of IEF in the CN structure. CNQDs are introduced into the CN plane, leading to directional flow of electrons due to the difference in the Fermi energy levels between the two components. The imbalance in charge across the

CN/CNQDs plane results in the formation of IEF. As shown in Fig. 6, the strong IEF drives the photogenerated electrons to migrate towards the lower Fermi energy level of the CNQDs end, and the photogenerated holes to migrate towards the CN end with a relatively high Fermi energy level. This minimizes carrier recombination and increases the photocatalytic hydrogen production activity of the CN/CNQDs photocatalyst (Fig. 7).

4. Conclusions

A highly efficient CN/CNQDs photocatalyst for hydrogen production was designed and prepared by implanting CNQDs into the planar structure of CN. The CN and CNQDs were connected by chemical bonding and the formation of continuous π -conjugate bonds enabled unimpeded transfer of photogenerated carriers. The strong IEF induced by the different Fermi energy levels acts as a direct driving force for the transfer of electrons and holes in the opposite directions, facilitating efficient separation of carriers in the photocatalyst. In the presence of Pt as a co-catalyst, the prepared CN/CNQDs-20–6 h photocatalyst achieved a photocatalytic hydrogen production rate of $10,921.8 \mu\text{mol/g}$ after 180 min of simulated sunlight illumination, which is 5.74 times higher than that of original CN, and exhibited good stability and reusability. This work provides a new way for the development of efficient atomic-level charge separation strategies for semiconductor-based photocatalysts.

CRediT authorship contribution statement

Xue Ma: Conceptualization, Formal analysis, Investigation, Methodology, Data curation, Writing – original draft; Writing – review & editing. **Hefa Cheng:** Conceptualization, Funding acquisition, Supervision, Writing – original draft, Writing – review & editing.

Declaration of Competing Interest

The authors declare that they have no known competing financial interests or personal relationships that could have appeared to influence the work reported in this paper.

Data Availability

Data will be made available on request.

Acknowledgments

The constructive comments of anonymous reviewers on an earlier version of this manuscript are greatly appreciated. This work was supported in parts by the Natural Science Foundation of China (Grant Nos. 41725015 and U2006212).

Appendix A. Supporting information

Supplementary data associated with this article can be found in the online version at [doi:10.1016/j.apcatb.2023.123101](https://doi.org/10.1016/j.apcatb.2023.123101).

References

- [1] C. Hepburn, E. Adlen, J. Beddington, E.A. Carter, S. Fuss, N. Mac Dowell, J.C. Minx, P. Smith, C.K. Williams, *Nature* 575 (2019) 87–97.
- [2] S. Xiang, Y. He, Z. Zhang, H. Wu, W. Zhou, R. Krishna, B. Chen, *Nat. Commun.* 3 (2012) 1–9.
- [3] H. Stančin, H. Mikulčić, X. Wang, N. Duić, *Renew. Sust. Energ. Rev.* 128 (2020), 109927.
- [4] X. Yin, R. Yang, G. Tan, S. Fan, *Science* 370 (2020) 786–791.
- [5] A. Hussain, S.M. Arif, M. Aslam, *Renew. Sust. Energ. Rev.* 71 (2017) 12–28.
- [6] F. Zhang, P. Zhao, M. Niu, J. Maddy, *Int. J. Hydrog. Energy* 41 (2016) 14535–14552.
- [7] Z. Lian, W. Wang, G. Li, F. Tian, K.S. Schanze, H. Li, *ACS Appl. Mater. Inter.* 9 (2017) 16959–16966.
- [8] W. Wang, S. Zhu, Y. Cao, Y. Tao, X. Li, D. Pan, D.L. Phillips, D. Zhang, M. Chen, G. Li, H. Li, *Adv. Funct. Mater.* 29 (2019) 1901958.
- [9] F. Dawood, M. Anda, G.M. Shafiullah, *Int. J. Hydrog. Energy* 45 (2020) 3847–3869.
- [10] Y. Kojima, *Int. J. Hydrog. Energy* 44 (2019) 18179–18192.
- [11] Y. Liu, X. Zeng, C.D. Easton, Q. Li, Y. Xia, Y. Yin, X. Hu, J. Hu, D. Xia, D. McCarthy, A. Deletic, C. Sun, J. Yu, X. Zhang, *Nanoscale* 12 (2020) 8775–8784.
- [12] Q. Zhou, S. Ma, S. Zhan, *Appl. Catal. B-Environ.* 224 (2018) 27–37.
- [13] M. Mofijur, T.M. Mahlia, A.S. Silitonga, H.C. Ong, M. Silakhori, M.H. Hasan, N. Putra, S.M.A. Rahman, Phase change materials (PCM) for solar energy usages and storage: an overview, *Energies* (2019) 3167.
- [14] E. Kabir, P. Kumar, S. Kumar, A.A. Adelodun, K.-H. Kim, *Renew. Sust. Energ. Rev.* 82 (2018) 894–900.
- [15] B. Han, Y.H. Hu, *Energy Sci. Eng.* 4 (2016) 285–304.
- [16] S. Guo, X. Li, J. Li, B. Wei, *Nat. Commun.* 12 (2021) 1343.
- [17] H. Hou, X. Zeng, X. Zhang, *Angew. Chem. Int. Ed.* 59 (2020) 17356–17376.
- [18] Y.-P. Yuan, L.-W. Ruan, J. Barber, S.C. Joachim Loo, C. Xue, *Energy Environ. Sci.* 7 (2014) 3934–3951.
- [19] C. Han, P. Su, B. Tan, X. Ma, H. Lv, C. Huang, P. Wang, Z. Tong, G. Li, Y. Huang, Z. Liu, *J. Colloid Interface Sci.* 581 (2021) 159–166.
- [20] Y. Xing, X. Wang, S. Hao, X. Zhang, X. Wang, W. Ma, G. Zhao, X. Xu, *Chin. Chem. Lett.* 32 (2021) 13–20.
- [21] S. Wang, J. Zhang, B. Li, H. Sun, S. Wang, *Energy Fuels* 35 (2021) 6504–6526.
- [22] X. Ma, G. Wang, L. Qin, J. Liu, B. Li, Y. Hu, H. Cheng, *Appl. Catal. B-Environ.* 288 (2021), 120025.
- [23] X. Ma, H. Cheng, *Appl. Catal. B-Environ.* 314 (2022), 121497.
- [24] M. Raaja Rajeshwari, S. Kokilavani, S. Sudheer Khan, *Chemosphere* 291 (2022), 132735.
- [25] X. Ma, H. Cheng, *J. Colloid Interface Sci.* 634 (2023) 32–43.
- [26] T. Wang, C. Nie, Z. Ao, S. Wang, T. An, *J. Mater. Chem. A* 8 (2020) 485–502.
- [27] J. Zhou, Y. Yang, C.-y. Zhang, *Chem. Commun.* 49 (2013) 8605–8607.
- [28] X. Wang, G. Sun, N. Li, P. Chen, *Chem. Soc. Rev.* 45 (2016) 2239–2262.
- [29] X. Hu, L. Zhong, C. Shu, Z. Fang, M. Yang, J. Li, D. Yu, *J. Am. Chem. Soc.* 142 (2020) 4621–4630.
- [30] W. Wang, J.C. Yu, Z. Shen, D.K.L. Chan, T. Gu, *Chem. Commun.* 50 (2014) 10148–10150.
- [31] X. He, Y. Gu, S. Ai, M. Xie, Q. Lu, Y. Wang, J. Wang, *Appl. Surf. Sci.* 462 (2018) 303–309.
- [32] Y. Chen, G. Huang, Y. Gao, Q. Chen, J. Bi, *Int. J. Hydrog. Energy* 47 (2022) 8739–8748.
- [33] P. Kumar, U.K. Thakur, K. Alam, P. Kar, R. Kisslinger, S. Zeng, S. Patel, K. Shankar, *Carbon* 137 (2018) 174–187.
- [34] B. Luo, Y. Hong, D. Li, Z. Fang, Y. Jian, W. Shi, A.C.S. Sustainable, *Chem. Eng.* 6 (2018) 14332–14339.
- [35] P. Ma, X. Zhang, C. Wang, Z. Wang, K. Wang, Y. Feng, J. Wang, Y. Zhai, J. Deng, L. Wang, K. Zheng, *Appl. Catal. B-Environ.* 300 (2022), 120736.
- [36] W. Che, W. Cheng, T. Yao, F. Tang, W. Liu, H. Su, Y. Huang, Q. Liu, J. Liu, F. Hu, Z. Pan, Z. Sun, S. Wei, *J. Am. Chem. Soc.* 139 (2017) 3021–3026.
- [37] K. Wang, J. Li, G. Zhang, *ACS Appl. Mater. Inter.* 11 (2019) 27686–27696.
- [38] H. Lin, K. Zhang, G. Yang, Y. Li, X. Liu, K. Chang, Y. Xuan, J. Ye, *Appl. Catal. B-Environ.* 279 (2020), 119387.
- [39] X. She, J. Wu, H. Xu, J. Zhong, Y. Wang, Y. Song, K. Nie, Y. Liu, Y. Yang, M.-T. F. Rodrigues, R. Vajtai, J. Lou, D. Du, H. Li, P.M. Ajayan, *Adv. Energy Mater.* 7 (2017) 1700025.
- [40] H. Yan, H. Yang, *J. Alloys, Compd* 509 (2011) 26–29.
- [41] Z. Xing, K. Dong, N. Pavlopoulos, Y. Chen, L. Amirav, *Angew. Chem. Int. Ed.* 60 (2021) 19413–19418.
- [42] J. Li, Y. Yin, E. Liu, Y. Ma, J. Wan, J. Fan, X. Hu, *J. Hazard. Mater.* 321 (2017) 183–192.
- [43] B. Fahimirad, A. Asghari, M. Rajabi, *Microchim. Acta* 184 (2017) 3027–3035.
- [44] B. Liu, L. Ye, R. Wang, J. Yang, Y. Zhang, R. Guan, L. Tian, X. Chen, *ACS Appl. Mater. Inter.* 10 (2018) 4001–4009.
- [45] Z. Mao, J. Chen, Y. Yang, D. Wang, L. Bie, B.D. Fahlman, *ACS Appl. Mater. Inter.* 9 (2017) 12427–12435.
- [46] M.K. Bhunia, K. Yamauchi, K. Takanabe, *Angew. Chem. Int. Ed.* 53 (2014) 11001–11005.
- [47] K. Schwinghammer, M.B. Mesch, V. Duppel, C. Ziegler, J. Senker, B.V. Lotsch, *J. Am. Chem. Soc.* 136 (2014) 1730–1733.
- [48] G. Liao, S. Chen, X. Quan, H. Yu, H. Zhao, *J. Mater. Chem.* 22 (2012) 2721–2726.
- [49] X. An, Q. Tang, H. Lan, H. Liu, X. Yu, J. Qu, H. Lin, J. Ye, *Angew. Chem. Int. Ed.* 61 (2022), e202212706.
- [50] C. Cheng, L. Mao, Z. Huang, J. Shi, B. Zheng, Y. Zhang, L. Guo, *J. Colloid Interface Sci.* 601 (2021) 220–228.
- [51] F. He, G. Chen, Y. Yu, S. Hao, Y. Zhou, Y. Zheng, *ACS Appl. Mater. Inter.* 6 (2014) 7171–7179.
- [52] I. Bertóti, M. Mohai, K. László, *Carbon* 84 (2015) 185–196.
- [53] C. Shan, X. Zhang, S. Ma, X. Xia, Y. Shi, J. Yang, *Colloids Surf. Physicochem. Eng. Asp.* 636 (2022), 128108.
- [54] Y. Guo, S. Huang, Y. Guo, Z. Ye, J. Nan, Q. Zhou, Y. Zhu, *Appl. Catal. B-Environ.* 312 (2022), 121388.
- [55] M. Jiang, C. Li, K. Huang, Y. Wang, J.-H. Liu, Z. Geng, X. Hou, J. Shi, S. Feng, *ACS Appl. Mater. Inter.* 12 (2020) 35113–35119.